

# Surface zeta potential and diamond growth on gallium oxide single crystal

Soumen Mandal<sup>a</sup>, Karsten Arts<sup>b</sup>, Harm C. M. Knoop<sup>b,c</sup>, Jerome Cuenca<sup>a</sup>,  
Georgina Klemencic<sup>a</sup>, Oliver A. Williams<sup>a</sup>

<sup>a</sup>*School of Physics and Astronomy, Cardiff University, Cardiff, UK*

<sup>b</sup>*Eindhoven University of Technology, 5612 AZ Eindhoven, Netherlands*

<sup>c</sup>*Oxford Instruments Plasma Technology, North End, Yatton, Bristol, BS49 4AP, UK*

---

## Abstract

In this work a strategy to grow diamond on  $\beta$ -Ga<sub>2</sub>O<sub>3</sub> has been presented. The  $\zeta$ -potential of the  $\beta$ -Ga<sub>2</sub>O<sub>3</sub> substrate was measured and it was found to be negative with an isoelectric point at pH  $\sim$  4.6. The substrates were seeded with mono-dispersed diamond solution for growth of diamond. The seeded substrates were etched when exposed to diamond growth plasma and globules of gallium could be seen on the surface. To overcome the problem  $\sim$ 100 nm of SiO<sub>2</sub> and Al<sub>2</sub>O<sub>3</sub> were deposited using atomic layer deposition. The nanodiamond seeded SiO<sub>2</sub> layer was effective in protecting the  $\beta$ -Ga<sub>2</sub>O<sub>3</sub> substrate and thin diamond layers could be grown. In contrast Al<sub>2</sub>O<sub>3</sub> layers were damaged when exposed to diamond growth plasma. The thin diamond layers were characterised with scanning electron microscopy and Raman spectroscopy. Raman spectroscopy revealed the diamond layer to be under compressive stress of 1.3 – 2.8GPa.

*Keywords:* Diamond, Zeta potential, Gallium oxide

---

## 1. Introduction

In the semiconducting industry silicon is the most widely used material. The band gap of Si is well suited for tailoring the conductivity from semi-insulating

---

*Email addresses:* mandals2@cardiff.ac.uk (Soumen Mandal),  
williams@cardiff.ac.uk (Oliver A. Williams)

to conducting. It also allows for the formation of both n-type and p-type material. As a result the application landscape of Si in the semiconducting industry is vast. Nonetheless, there are areas of applications in which Si as a material is not well suited. For example, many high temperature applications are dependent on the breakdown electric field strength ( $E_{br}$ ), which has a strong correlation with the bandgap. To overcome the limitations of silicon in high temperature applications, many wide bandgap ( $2.0 \text{ eV} \leq E_g \leq 7.0 \text{ eV}$ )[1] compound semiconductors like SiC ( $E_g = 2.4 - 3.2 \text{ eV}$ )[1] and GaN( $E_g = 3.39 \text{ eV}$ )[2] have been developed. Even as wide band gap electronics based on SiC and GaN are maturing, newer materials with wider band gaps ( $E_g > 3.4 \text{ eV}$ ) are appearing on the horizon. One of the ways to compare different semiconductors is through figures of merit. For low frequency operations, the Baliga figure of merit(BFM)[3] is widely used and for high frequency operations Johnsons figure of merit(JFM)[4] is widely accepted. Based on BFM of different wide band gap materials,  $\beta\text{-Ga}_2\text{O}_3$ , AlN, diamond and c-BN are some of the materials that are considered superior to GaN and SiC[5]. Of these four materials,  $\beta\text{-Ga}_2\text{O}_3$  has attracted a lot of attention in recent times[5, 6, 7, 8, 9, 10], mostly due to availability of large substrates. These large substrates are grown by several melt growth methods like float zone[11, 12], Czochralski[13, 14], Bridgman[15, 16] and edge-defined film-fed growth (EFG)[6, 17, 18] .

While the study in growth of large substrates is an on-going topic, researchers have already demonstrated devices made from gallium oxide[19, 20, 21, 22, 23, 24, 25, 26, 27]. The demonstrated devices point towards promising advantages in gallium oxide over traditional wide band gap semiconductors like SiC and GaN. However, as with most high power devices, thermal management in gallium oxide devices, with its low thermal conductivity ( $10\text{-}30 \text{ W/mK}$ )[28], is a major bottle neck in the development of technology based on this material[9]. It is a well known fact that higher operation temperature in high power devices can lead to significantly lower lifetimes[29, 30]. One way researchers have overcome this problem is by exfoliating gallium oxide[26, 27, 31] or by growing gallium oxide on single crystal diamond(thermal conductivity  $\sim 2000 \text{ W/mK}$ )

substrates[32]. Another approach that has been recently demonstrated is low temperature bonding of single crystal diamond on  $\beta$ -Ga<sub>2</sub>O<sub>3</sub> [33]. The major drawback in all these approaches is the small area of the resulting heterostructure for device fabrication. Availability of large area single crystal is currently very limited[34] or very expensive. An alternative approach can be direct bonding of large  $\beta$ -Ga<sub>2</sub>O<sub>3</sub> crystals to chemical mechanical polished[35, 36, 37] flat polycrystalline diamond films. This technique is also not straightforward and will involve non-trivial sample surface preparations. A solution to the thermal management problem can be to grow a thick diamond layer on  $\beta$ -Ga<sub>2</sub>O<sub>3</sub> single crystal similar to what we have shown in the past on AlN thin films[38].

The growth of diamond on non-diamond substrates is not trivial. The surface energy of diamond is  $\sim 6 \text{ J/m}^2$ [39]. In comparison the surface energy of silicon, which is most commonly used substrate, is  $\sim 1.5 \text{ J/m}^2$  [40]. Due to this large surface energy difference heteroepitaxial growth of diamond is not possible[41, 42] and results in only isolated diamond islands. On silicon the density of such islands are of the order of  $10^4 - 10^5 \text{ cm}^{-2}$ . With a surface energy of  $\sim 1 \text{ J/m}^2$  [43] for  $\beta$ -Ga<sub>2</sub>O<sub>3</sub>, similar island formations are expected for heteroepitaxial growth. Hence, a seeding/nucleation technique is essential for growth of diamond films on gallium oxide surfaces. An additional issue with growth of diamond on non-diamond substrates using typical CVD approaches is the exposure of the sample to chemically reactive H<sub>2</sub> plasma. For example, there are well-known challenges for depositing diamond on GaN[38]. Additionally, H<sub>2</sub> plasmas are also known to cause surface damage to  $\beta$ -Ga<sub>2</sub>O<sub>3</sub>[44]. In this work, growth of diamond on  $\beta$ -Ga<sub>2</sub>O<sub>3</sub> substrates has been demonstrated. The  $\zeta$  - potential of the substrates have been measured to determine the best seeding solution. It was found that the substrates disintegrate when exposed to plasma during diamond growth leaving behind globules of gallium. To overcome this, a thin layer of SiO<sub>2</sub> and Al<sub>2</sub>O<sub>3</sub> was deposited as a buffer layer. The  $\zeta$ -potential of the buffer layers were also measured. Thin diamond films were grown (250nm) and characterised using scanning electron microscopy. Also, the film stresses were characterised using Raman spectroscopy. For deposition of thick diamond

layers alternative strategies will have to be designed to manage the stress at the interface, which will be the basis of further studies.

## 2. Experiment

When a solid is immersed in a liquid it acquires a surface charge which is compensated by ions of opposite charge or counterions that are loosely bound to the surface. The surface charge is formed due to adsorbed ions on the surface of solid and that forms the first layer. The counterions are then attracted towards the surface due to Coulomb attraction and are part of a second layer called diffuse layer. The first layer is immobile with respect to solid. The surface charges also generate a potential which decays with distance from the solid surface.  $\zeta$ -potential is defined as the potential at the boundary of the immobile and mobile liquid with respect to rest of the liquid. For measuring  $\zeta$ -potential it is essential to measure the charge on the counterions. If a channel is formed between two solid surfaces and an electrolyte is passed through the channel, the counterions experience a shearing force and move along with the electrolyte[45]. As a result a charge separation is formed between the inlet and outlet of the channel. This leads to formation of an electric potential known as streaming potential. First suggested by Van Wagenen et al.[45], it has been used for determination of  $\zeta$ -potential of variety of surfaces[38, 46, 47, 48, 49, 50, 51, 52]. The Helmholtz-Smoluchowski equation gives a relation between  $\zeta$ -potential and streaming current/potential[53]. By measuring the change in streaming current/potential as a function of electrolyte pressure the  $\zeta$ -potential can be determined. The  $\zeta$ -potential of  $\beta$ -Ga<sub>2</sub>O<sub>3</sub>, SiO<sub>2</sub> and Al<sub>2</sub>O<sub>3</sub> coated  $\beta$ -Ga<sub>2</sub>O<sub>3</sub>, sapphire and quartz were measured using Surpass<sup>TM</sup> 3 electrokinetic analyzer. In the present work the channel width was kept between 90-110  $\mu$ m. The electrolyte was 10<sup>-3</sup> M solution of KCl in DI water with electrolyte pressure varying between 200 and 600 mbar. The pH of the electrolyte was varied by addition of 0.1M NaOH and 0.1M HCl solution with the inbuilt titrator in Surpass<sup>TM</sup> 3.

The  $\sim 100$  nm  $\text{SiO}_2$  and  $\text{Al}_2\text{O}_3$  layers were grown by atomic layer deposition (ALD), using an Oxford Instruments FlexAL reactor[54]. Both layers were grown using 1100 ALD cycles and a target temperature setpoint of 300 °C. The  $\text{SiO}_2$  layer was grown using  $\text{SiH}_2(\text{NEt}_2)_2$  (bis(diethylamino)silane) as precursor and  $\text{O}_2$  plasma as coreactant, where the  $\text{O}_2$  plasma was generated by an inductively coupled plasma source. Purely thermally-driven ALD was employed for the growth of  $\text{Al}_2\text{O}_3$ , using  $\text{Al}(\text{CH}_3)_3$  (trimethylaluminum) and  $\text{H}_2\text{O}$ . The thicknesses of the deposited  $\text{SiO}_2$  and  $\text{Al}_2\text{O}_3$  layers were measured by spectroscopic ellipsometry (SE), using a M-2000D Spectroscopic Ellipsometer of J.A. Woollam Co. The SE measurements were performed ex-situ on silicon substrates (Czochralski silicon (100) with  $\sim 1.6$  nm native oxide) that were processed alongside the  $\beta\text{-Ga}_2\text{O}_3$  substrates. A Cauchy dispersion model was used for fitting the SE data[55]. The film thicknesses were measured to be 89 nm for the  $\text{SiO}_2$  layer and 111 nm for the  $\text{Al}_2\text{O}_3$  layer. Moreover, the refractive indices of the films (at 632.8 nm) were measured as 1.45 for  $\text{SiO}_2$  and 1.65 for  $\text{Al}_2\text{O}_3$ .

After  $\zeta$ -potential measurements the substrates were seeded with mono-dispersed diamond solution. The details of the seeding process can be found here[42]. The seeded wafers were then introduced in a Carat Systems SDS6U microwave plasma chemical vapour deposition(MPCVD) systems. The growth was done in two steps, that is incubation and growth. The growth of diamond by MPCVD is essentially a complex process of growth and etching of all forms of carbon with non-diamond carbon surviving only in negligible quantities. The nanodiamond seeds used for seeding are typically 5nm in size. As a result they have considerable surface to volume ratio resulting in large proportion of non-diamond carbon[41] at the surface which are easily etched in the plasma. The incubation step, lasting for 3-10 mins, is used for fast growth of seeds so that they are not fully etched away during initial stages of growth. For the incubation step a gas mixture of 5%  $\text{CH}_4/\text{H}_2$  and 50 torr chamber pressure with 3.7 kW microwave power was used. The incubation period was 5 minutes and the gas flow was maintained at 500 sccm. After the incubation period the gas mixture was modified to 3%  $\text{CH}_4/\text{H}_2$ . The total time for the growth was 40 mins and the growth

temperature was 630 °C as recorded by dual wavelength Williamson pyrometer. After growth the sample was slowly cooled in hydrogen plasma. The substrates, diamond layers and oxide coating were analysed using a Horiba LabRAM HR Evolution equipped with SynapsePlus Back-Illuminated Deep Depletion (BIDD) CCD. The spectroscopy is equipped with three lasers having wavelengths of 473, 532 and 660nm. Data from all three lasers have been included in this work. A Hitachi SU8200 series scanning electron microscope (SEM) operating at 10 kV and working distances between 9 and 11 mm was used for imaging the samples after growth.  $(\bar{2}01)$   $\beta$ -Ga<sub>2</sub>O<sub>3</sub> substrates used in this work were commercially sourced from Tamura Corporation. The substrates were single side chemical mechanical polished. 10X10mm and 5X5mm pieces were cut from a 2" wafer for growth of diamond.

### 3. Results and Discussion

#### 3.1. Zeta potential measurement

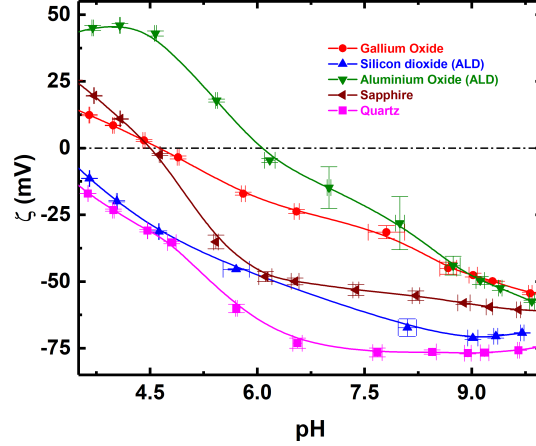


Figure 1: Zeta potential vs pH for  $\beta$ -Ga<sub>2</sub>O<sub>3</sub> crystal. The figure also show the zeta potential of deposited buffer layers namely, SiO<sub>2</sub> and Al<sub>2</sub>O<sub>3</sub>. The zeta potential of quartz and sapphire are shown for comparison as well. The solid lines are a guide to the eye. The dashed black line has been put to mark the isoelectric point.

The determination of the  $\zeta$ -potential of a non-diamond substrate, which is

directly related to surface charge, is essential for the determination of the type of seed solution needed for high seed density. It is possible to create diamond seed solution with positive or negative surface charge in water[41, 42, 56]. For high seed density seed solution with charged particles opposite to charges on substrate surface are essential. Figure 1 shows the  $\zeta$ -potential as a function of electrolyte pH for  $\beta$ -Ga<sub>2</sub>O<sub>3</sub> along with potentials of ALD deposited SiO<sub>2</sub>, Al<sub>2</sub>O<sub>3</sub>, quartz and sapphire. The  $\zeta$ -potential of  $\beta$ -Ga<sub>2</sub>O<sub>3</sub> is negative beyond the isoelectric point around pH  $\sim$  4.6. This is in contrast to gallium oxide nanoparticles which have an isoelectric point of pH $\sim$ 9 [57]. However,  $\zeta$ -potential of single crystal  $\beta$ -Ga<sub>2</sub>O<sub>3</sub> plate is similar to the  $\zeta$ -potential for Ga faced GaN[49] where as, N-face GaN has more negative  $\zeta$ -potential. The higher negative  $\zeta$  of N-faced GaN could be down to higher amounts of adsorbed oxygen on the surface. However, the main point of interest for seeding is around pH 6-7. In this range the  $\zeta$  potential of  $\beta$ -Ga<sub>2</sub>O<sub>3</sub> is negative with a value between -20 and -30mV. This means that for high seed density H-terminated diamond seed solution is needed[56]. The substrates were seeded by dipping in H-terminated nanodiamond solution. The seeded substrates were then exposed to H<sub>2</sub>/CH<sub>4</sub> plasma for diamond growth. As soon as the substrates were exposed to the plasma, immediate damage to the  $\beta$ -Ga<sub>2</sub>O<sub>3</sub> surface could be observed. On closer examination under SEM (see later in figure 2), globules of gallium metal was observed.

To overcome the damage to the substrate surface from the plasma, it was encapsulated with a dielectric coating. For the purpose of the current study, SiO<sub>2</sub> and Al<sub>2</sub>O<sub>3</sub> were chosen. Thin layers of the coatings were deposited with ALD. For measuring the zeta potential of the deposited coatings, quartz pieces were included during the deposition of the dielectrics on  $\beta$ -Ga<sub>2</sub>O<sub>3</sub>. The  $\zeta$  potential of 100nm ALD deposited dielectrics are shown in figure 1. For comparison  $\zeta$ -potential of the quartz (SiO<sub>2</sub>) and sapphire (Al<sub>2</sub>O<sub>3</sub>) are also shown. While SiO<sub>2</sub> has negative  $\zeta$ -potential over the whole measurement range (pH  $\sim$  3-10), Al<sub>2</sub>O<sub>3</sub> has isoelectric point at pH  $\sim$  6 and has negative  $\zeta$ -potential beyond that point. In the case of SiO<sub>2</sub> the  $\zeta$ -potential is not dependent on whether it is in the form of quartz, thin layer or nanoparticles[58]. In contrast, for Al<sub>2</sub>O<sub>3</sub>

it has a strong dependence on whether it is in the form of sapphire (isoelectric point  $\text{pH} \sim 4.5$ ), thin film (isoelectric point  $\text{pH} \sim 6$ ) or nanoparticles (isoelectric point  $\text{pH} \sim 9$ )[59], which is similar to what is seen for gallium oxide. As before the substrates with dielectric encapsulation were seeded with H-terminated diamond seed solution. The seeded samples were exposed to diamond growth conditions. Thin diamond films could be grown on substrates encapsulated with  $\text{SiO}_2$ . The  $\text{Al}_2\text{O}_3$  thin layer disintegrated on exposure to plasma and exposed the underlying  $\beta\text{-Ga}_2\text{O}_3$  surface. This is probably due to large thermal mismatch between  $\text{Al}_2\text{O}_3$  layer and  $\beta\text{-Ga}_2\text{O}_3$ . Alternatively, it is also possible that  $\text{Al}_2\text{O}_3$  is easily etched[60] in  $\text{CH}_4/\text{H}_2$  plasma while  $\text{SiO}_2$  can act as a mask[61] in the same environment.

### 3.2. Scanning Electron Microscopy

Figure 2A shows the scanning electron microscope images for diamond thin films grown on  $\text{SiO}_2$  coated  $\beta\text{-Ga}_2\text{O}_3$ . A fully coalesced film with grain sizes of the order of 250nm can be clearly seen. Panel B in the image shows sample surface coated with  $\text{Al}_2\text{O}_3$ . The  $\text{Al}_2\text{O}_3$  coating has completely disintegrated in the diamond growth plasma. Small flakes of  $\text{Al}_2\text{O}_3$  can be clearly seen in the image. Once the  $\text{Al}_2\text{O}_3$  layer disintegrates, the  $\beta\text{-Ga}_2\text{O}_3$  surface is exposed to plasma and small gallium globules are formed. Such globules were also seen for samples that were not coated with a protective oxide.

### 3.3. Raman spectroscopy

In this section we will discuss the Raman spectra of  $\beta\text{-Ga}_2\text{O}_3$ ,  $\text{SiO}_2$  coated  $\beta\text{-Ga}_2\text{O}_3$  and diamond grown on  $\text{SiO}_2$  coated  $\beta\text{-Ga}_2\text{O}_3$ . A detailed comparison between  $\beta\text{-Ga}_2\text{O}_3$  and  $\text{SiO}_2$  coated  $\beta\text{-Ga}_2\text{O}_3$  will be done to investigate the effects of the  $\text{SiO}_2$  layer on the Raman modes of  $\beta\text{-Ga}_2\text{O}_3$ .  $\beta\text{-Ga}_2\text{O}_3$  unit cell has 30 phonon modes [62, 63], of these only 27 are optically active. Amongst the optically active modes 15 are Raman active which have  $A_g$  and  $B_g$  symmetry. Since only the modes with  $A_g$  and  $B_g$  symmetry are Raman active in  $\beta\text{-Ga}_2\text{O}_3$ ,  $A_g^{(1)}$  will be denoted simply as A1, where  $A_g^{(1)}$  has a spectral position at 111



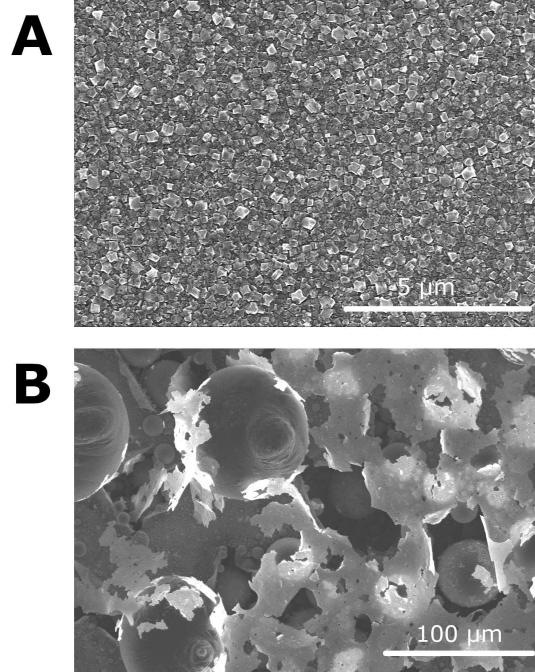


Figure 2: A. Scanning electron microscope image of thin diamond film grown on  $\text{SiO}_2$  coated  $\beta\text{-Ga}_2\text{O}_3$ . B. Image of the  $\text{Al}_2\text{O}_3$  coated  $\beta\text{-Ga}_2\text{O}_3$  surface after exposure to diamond growth condition. Tiny gallium globules along with flakes of  $\text{Al}_2\text{O}_3$  can be clearly seen.

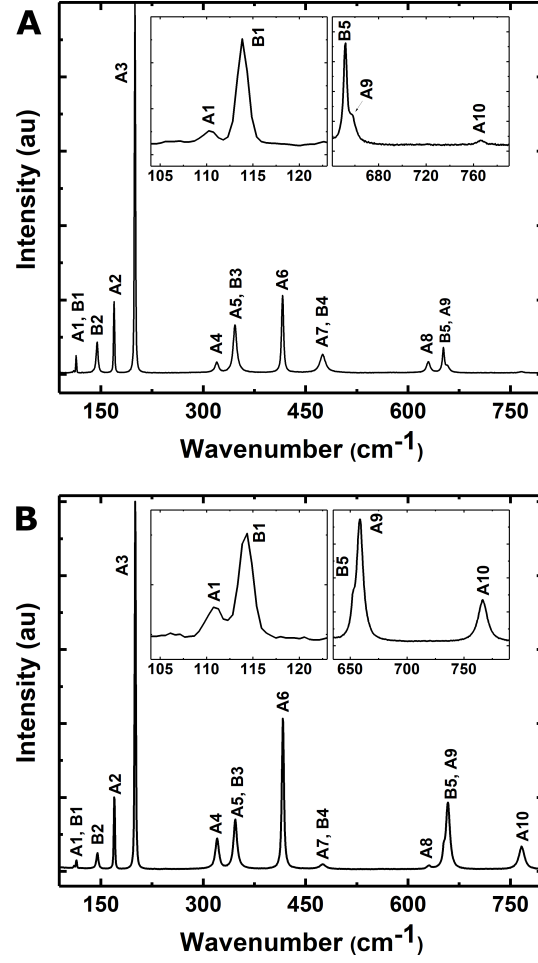


Figure 3: Raman spectroscopy data is shown for A)  $\beta\text{-Ga}_2\text{O}_3$  and B)  $\text{SiO}_2$  covered  $\beta\text{-Ga}_2\text{O}_3$ . The common peaks are marked in the figure. The inset shows the magnified view of A1, B1 peaks (left inset) and B5, A9 and A10 peaks (right inset). Note the change in relative intensities of various peaks in bare substrate and  $\text{SiO}_2$  covered substrate, specifically A6, B5, A9 and A10. The data was taken using 532 nm laser.

$\text{cm}^{-1}$  according to Kranert et al.[63]. The rest of the Raman modes will follow similar convention throughout this article. The Raman spectra for bare  $\beta\text{-Ga}_2\text{O}_3$  substrate and 100nm  $\text{SiO}_2$  covered  $\beta\text{-Ga}_2\text{O}_3$  is shown in figure 3A and B respectively. The data was taken using 532 nm laser. The data taken with 473 and 660nm lasers are presented in figures S1 and S2 respectively. The common peaks in  $\beta\text{-Ga}_2\text{O}_3$  are marked in the figure. The peak positions of the different modes for both samples are listed in table 1 along with their full width at half maximum (FWHM). The peak positions have been determined by fitting a Lorentz function to the Raman data[63]. While the bare substrate data fits well with the Lorentzian peak fit, some peaks in  $\text{SiO}_2$  covered substrate are best fitted with Voigt function. The results of the peak fitting using Voigt function are shown in table S1. The FWHM of the peaks fitted with Voigt function have been calculated on the basis of definition given by Olivero et al.[64]. GLmix in the table (Table S1) defines the proportion of Lorentzian character of the Voigt function[65]. The relative intensities (Rel. Int.) of the peaks are calculated from the area of the fitted curves and has been normalised with respect to A3 peak. The peaks of B3 and B4 modes are very close to A5 and A7 respectively and is indistinguishable from each other. Hence, the modes A5, B3 and A7, B4 are represented together in the table. The relative intensities on  $\beta\text{-Ga}_2\text{O}_3$  show trends similar to that shown by Kranert et al.[63] In contrast, there is considerable deviation in the intensity trends for  $\text{SiO}_2$  covered  $\beta\text{-Ga}_2\text{O}_3$  and follows more closely the intensity trend of parallel polarisation along the  $[102]$  direction on  $(\bar{2}01)$   $\beta\text{-Ga}_2\text{O}_3$ .

The peaks in the data can be divided into three distinct regions[62]. First region are the peaks below  $200 \text{ cm}^{-1}$ , the second region are the peaks between  $300$  and  $500 \text{ cm}^{-1}$  and the third one are the peaks above  $600 \text{ cm}^{-1}$ . The peaks below  $200 \text{ cm}^{-1}$  are associated with vibrations of the tetrahedra chains[62] i.e. small amplitudes and have narrow widths of  $\sim 3 \text{ cm}^{-1}$ . In this region the FWHM of the peaks are slightly wider for  $\text{SiO}_2$  covered  $\beta\text{-Ga}_2\text{O}_3$  and this trend is seen for most peaks. The intensity trend is similar except for the B1 and B2 modes having lower intensities. However, the intensity trend for the peaks beyond

Raman mode	$\beta$ -Ga <sub>2</sub> O <sub>3</sub>			SiO <sub>2</sub> on $\beta$ -Ga <sub>2</sub> O <sub>3</sub>		
	Peak Center	FWHM	Rel. Int.	Peak Center	FWHM	Rel. Int.
A1	109.95	2.30	8.70	110.67	2.27	7.66
B1	113.89	1.31	35.29	114.24	1.68	19.67
B2	144.54	3.15	144.97	144.93	3.39	72.91
A2	169.44	1.67	189.92	169.84	1.84	195.13
A3	199.99	1.70	1000	200.41	1.90	1000
A4	319.85	5.69	83.19	320.36	5.94	241.01
A5, B3	346.56	6.03	419.67	347.00	6.06	398.24
A6	416.28	3.27	378.74	416.75	3.39	701.80
A7, B4	475.03	9.76	256.77	475.15	10.28	62.19
A8	629.77	6.46	101.68	630.59	7.02	28.81
B5	651.88	3.49	121.95	652.34	3.47	54.73
A9	658.04	6.61	51.97	658.50	6.78	604.38
A10	766.20	8.43	13.70	766.53	9.69	295.99

Table 1: Peak positions, FWHM and relative intensity with respect to A3 of Raman peaks for  $\beta$ -Ga<sub>2</sub>O<sub>3</sub> and SiO<sub>2</sub> coated  $\beta$ -Ga<sub>2</sub>O<sub>3</sub>. The peak positions and FWHM are in cm<sup>-1</sup>.

200  $\text{cm}^{-1}$  is completely different for  $\beta\text{-Ga}_2\text{O}_3$  and  $\text{SiO}_2$  covered  $\beta\text{-Ga}_2\text{O}_3$ . In this region the peaks are broader ( $\text{FWHM} > 3 \text{ cm}^{-1}$ ). The modes above 200  $\text{cm}^{-1}$  correspond to bending and stretching modes or internal vibrations of the tetrahedra groups. The presence of the  $\text{SiO}_2$  layer on top of  $\beta\text{-Ga}_2\text{O}_3$  seem to have disproportionate effect on these modes. Finally, Raman spectra of diamond film grown on  $\text{SiO}_2$  covered  $\beta\text{-Ga}_2\text{O}_3$  has been taken and the data is presented in figure 4. The data was taken with 532 nm laser. The spectra from  $\beta\text{-Ga}_2\text{O}_3$ ,  $\text{SiO}_2$  coated  $\beta\text{-Ga}_2\text{O}_3$  and diamond taken with 532nm laser are presented together in figure S3 for comparison.

The Raman spectroscopy data for diamond thin film on  $\text{SiO}_2$  coated  $\beta\text{-Ga}_2\text{O}_3$ , shown in figure 4A, shows a clear diamond peak. The data was taken with 532 nm excitation laser and a straight line luminescence background was subtracted[66] before presenting the data in the figure. Data was also taken with 473 and 660 nm excitation. The data taken at 473 nm also showed luminescence background, however the background was absent for the data taken at 660 nm[67]. The  $\beta\text{-Ga}_2\text{O}_3$  Raman peaks were present in all three dataset and the same are shown in figure S4. The figure also shows the background straight line subtracted for the data in figure 4. The commonly observed peaks in thin diamond films are marked in figure 4. The small shoulder around 1350  $\text{cm}^{-1}$  is associated with the D peak from amorphous carbon [68, 69, 70]. The peak at around 1332  $\text{cm}^{-1}$  is the diamond peak[71, 72], however, it is clearly shifted towards higher wavenumbers and is heavily convoluted with additional bands. This is likely due to stress in the diamond thin film[73, 74, 75, 76, 77]. Accurate determination of the stress magnitude requires appropriate deconvolution of the spectra. Gries et al. [78] demonstrated that multiple types were required to resolve the spectra; 1 Gaussian for non-diamond carbon and 3 Lorentzians for diamond peaks in various stress states. In the simplest way, resolving the spectra between 1300 and 1400  $\text{cm}^{-1}$  for one Lorentzian and one Gaussian profiles yield peak positions of 1336  $\text{cm}^{-1}$  and 1359.4  $\text{cm}^{-1}$  for the diamond and D peaks, respectively. In a similar approach to Gries et al.[78], the spectra in this work obtained a better fit (higher  $R^2$  and lower  $\chi^2$ ) using 2 Lorentzian peaks to

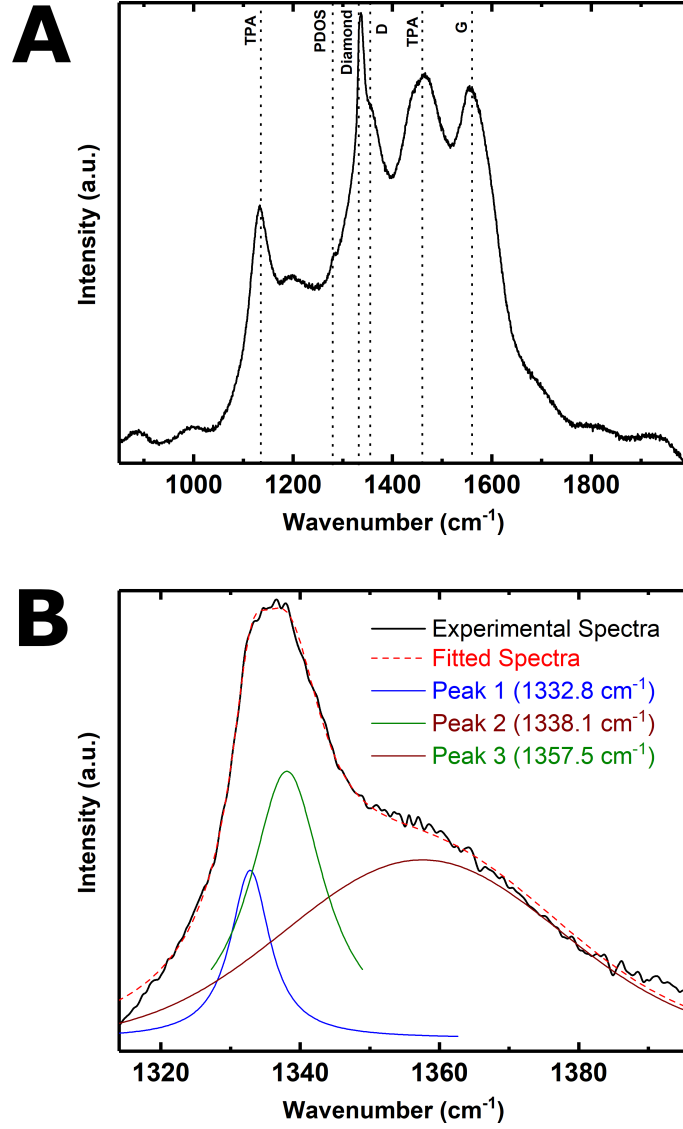


Figure 4: A. Raman spectroscopy data is shown for diamond thin film grown on  $\text{SiO}_2$  coated  $\beta\text{-Ga}_2\text{O}_3$ . The positions of common Raman peaks seen in diamond thin films are marked in the figure. The data was taken using 532 nm laser. B. The zoomed in view of the diamond peak is shown along with the fitted curves. The peak has been fitted with two Lorentzian and one Gaussian curve.

resolve the diamond contributions (1332.8 and 1338.1 cm<sup>-1</sup>) and a Gaussian peak to resolve the D peak (1357.5 cm<sup>-1</sup>). Further increment in number of peaks results in non-convergence of the fitting parameters and leads to unfeasible results. Figure 4B shows the zoomed view of the diamond peak and D peak from amorphous carbon. The deconvoluted peaks along with the calculated curve are shown in the figure.

Considering the fits to the diamond peak in figure 4B the shift in the peak is between 4-6 cm<sup>-1</sup>, depending on whether one considers the resolved or unresolved peak. Various researchers have estimated different stress coefficients for Raman peak shifts. Boppart et al.[79] estimated the stress coefficient for Raman line shifts to be around 0.38 GPa/cm<sup>-1</sup> by measuring the shifts in Raman line for a diamond crystal under pressure. Knight et al. [73] concluded a similar coefficient of 0.42 GPa/cm<sup>-1</sup> by measuring stress in diamond films. However, Yoshikawa et al. [80, 81] used the value of 2.63 GPa/cm<sup>-1</sup> for their results assuming only hydrostatic stress. Windischmann et al.[75] used a value of 0.39 GPa/cm<sup>-1</sup>, however the postulated that films grown on substrates are under biaxial stress, hence the coefficient is 1.5 times larger resulting in a coefficient of 0.59 GPa/cm<sup>-1</sup>. These figures were later disputed by Anastassakis [76]. Based on equations given by Anastassakis [76], the stress in the diamond films presented in this work is estimated to be between 1.3 and 2.8 GPa (assuming isotropic stress), which is closer to the results of Boppart et al.[79] and Knight et al.[73]. The stress along with adhesion strength between various components of the stack consisting of  $\beta$ -Ga<sub>2</sub>O<sub>3</sub>, SiO<sub>2</sub> and diamond will determine if a film will stick on the substrate. It should be noted that the stress between layers is thickness dependent[82]. In the case of diamond on SiO<sub>2</sub> covered  $\beta$ -Ga<sub>2</sub>O<sub>3</sub> the film thickness is limited to 250nm.

Figure 4A also shows peaks at  $\sim 1150$  and  $\sim 1450$  cm<sup>-1</sup>. These are associated with the transpolyacetylene present at grain boundaries and diamond surface[83]. The peak around  $\sim 1560$  cm<sup>-1</sup> is associated with G peak from amorphous carbon[69, 70]. Apart from these a small shoulder can be seen around  $\sim 1280$  cm<sup>-1</sup>. This is associated with phonon density of states (PDOS)

in diamond[84, 69]. Small bumps around 900, 1000 and 1220  $\text{cm}^{-1}$  can also be seen which can also be attributed to PDOS of diamond[84].

#### 4. Conclusion

In conclusion, the  $\zeta$ -potential of  $\beta\text{-Ga}_2\text{O}_3$  has been presented. The  $\zeta$ -potential was found to be negative above  $\text{pH} \sim 4.6$ , enabling the use of H-terminated diamond seed solution for seeding of the surface. The  $\zeta$ -potential is similar to that of Ga-faced gallium nitride. In contrast gallium oxide nanoparticles have largely positive  $\zeta$ -potential with isoelectric point at  $\text{pH} \sim 9$ [57]. A method for growing diamond on  $\beta\text{-Ga}_2\text{O}_3$  crystal has also been detailed. It was found that direct growth of diamond on  $\beta\text{-Ga}_2\text{O}_3$  is not possible with MPCVD. As a result, thin layer of  $\text{Al}_2\text{O}_3$  and  $\text{SiO}_2$  were deposited on  $\beta\text{-Ga}_2\text{O}_3$  before diamond deposition. Upon seeding with diamond solution,  $\text{SiO}_2$  layer survived the diamond growth condition and resulted in a thin diamond layer. In contrast the seeded  $\text{Al}_2\text{O}_3$  layer of similar thickness was completely destroyed when exposed to diamond growth conditions. Raman measurements were done on  $\beta\text{-Ga}_2\text{O}_3$ , coated  $\beta\text{-Ga}_2\text{O}_3$  and diamond on coated  $\beta\text{-Ga}_2\text{O}_3$ . It was found that the diamond layer is under considerable amount of stress and this is due to the mismatch in thermal expansion coefficient between  $\beta\text{-Ga}_2\text{O}_3$  and diamond. Further work is needed to manage the interfacial stress between diamond and coated  $\beta\text{-Ga}_2\text{O}_3$  for growth of thick diamond layer on  $\beta\text{-Ga}_2\text{O}_3$ .

#### 5. Acknowledgment

This project has been supported by Engineering and Physical Sciences Research Council under programme Grant GaN-DaME (EP/P00945X/1). The metadata for the results presented in this paper can be found [here](#)().

#### References

- [1] J. Casady, R. Johnson, Status of silicon carbide (SiC) as a wide-bandgap semiconductor for high-temperature Solid-State Electronics 39 (10) (1996) 1409–1422.



doi:10.1016/0038-1101(96)00045-7.

URL [http://dx.doi.org/10.1016/0038-1101\(96\)00045-7](http://dx.doi.org/10.1016/0038-1101(96)00045-7)

- [2] U. Mishra, Shen Likun, T. Kazior, Yi-Feng Wu, GaN-Based RF Power Devices and Amplifiers, Proceedings of the IEEE 96 (2) (2008) 287–305. doi:10.1109/JPROC.2007.911060.  
URL <http://dx.doi.org/10.1109/JPROC.2007.911060>
- [3] B. J. Baliga, Semiconductors for high-voltage, vertical channel field-effect transistors, Journal of Applied Physics 53 (3) (1982) 1759–1764.  
doi:10.1063/1.331646.  
URL <http://dx.doi.org/10.1063/1.331646>
- [4] E. O. Johnson, Physical Limitations on Frequency and Power Parameters of Transistors, RCA Reviews 26 (1965) 163–177.
- [5] J. Y. Tsao, S. Chowdhury, M. A. Hollis, D. Jena, N. M. Johnson, K. A. Jones, R. J. Kaplar, S. Rajan, C. G. Van de Walle, E. Bellotti, C. L. Chua, R. Collazo, M. E. Coltrin, J. A. Cooper, K. R. Evans, S. Graham, T. A. Grotjohn, E. R. Heller, M. Higashiwaki, M. S. Islam, P. W. Juodawlkis, M. A. Khan, A. D. Koehler, J. H. Leach, U. K. Mishra, R. J. Nemanich, R. C. N. Pilawa-Podgurski, J. B. Shealy, Z. Sitar, M. J. Tadjer, A. F. Witulski, M. Wraback, J. A. Simmons, Ultrawide-Bandgap Semiconductors: Research Opportunities and Challenges, Advanced Electronic Materials 4 (1) (2018) 1600501.  
doi:10.1002/aelm.201600501.  
URL <http://dx.doi.org/10.1002/aelm.201600501>
- [6] M. Higashiwaki, K. Sasaki, H. Murakami, Y. Kumagai, A. Koukitu, A. Kuramata, T. Masui, S. Yamakoshi, Recent progress in Ga<sub>2</sub>O<sub>3</sub> power devices, Semiconductor Science and Technology 31 (3) (2016) 034001. doi:10.1088/0268-1242/31/3/034001.  
URL <http://dx.doi.org/10.1088/0268-1242/31/3/034001>

- [7] S. J. Pearton, F. Ren, M. Tadjer, J. Kim, Perspective: Ga<sub>2</sub>O<sub>3</sub> for ultra-high power rectifiers and MOSFETS, Journal of Applied Physics 124 (22) (2018) 220901. doi:10.1063/1.5062841. URL <http://dx.doi.org/10.1063/1.5062841>
- [8] S. J. Pearton, J. Yang, P. H. Cary, F. Ren, J. Kim, M. J. Tadjer, M. A. Mastro, A review of Ga<sub>2</sub>O<sub>3</sub> materials, processing, and devices, Applied Physics Reviews 5 (1) (2018) 011301. doi:10.1063/1.5006941. URL <http://dx.doi.org/10.1063/1.5006941>
- [9] M. Higashiwaki, G. H. Jessen, Guest Editorial: The dawn of gallium oxide microelectronics, Applied Physics Letters 112 (6) (2018) 060401. doi:10.1063/1.5017845. URL <http://dx.doi.org/10.1063/1.5017845>
- [10] H. W. Xue, Q. M. He, G. Z. Jian, S. B. Long, T. Pang, M. Liu, An Overview of the Ultrawide Bandgap Ga<sub>2</sub>O<sub>3</sub> Semiconductor-Based Schottky Barrier Diode for Power Electronics, Nanoscale Research Letters 13 (2018) 290. doi:10.1186/s11671-018-2712-1. URL <http://dx.doi.org/10.1186/s11671-018-2712-1>
- [11] E. G. Villora, K. Shimamura, Y. Yoshikawa, K. Aoki, N. Ichinose, Large-size  $\beta$ -Ga<sub>2</sub>O<sub>3</sub> single crystals and wafers, Journal of Crystal Growth 270 (3-4) (2004) 420–426. doi:10.1016/j.jcrysgro.2004.06.027. URL <http://dx.doi.org/10.1016/j.jcrysgro.2004.06.027>
- [12] S. Ohira, M. Yoshioka, T. Sugawara, K. Nakajima, T. Shishido, Fabrication of hexagonal GaN on the surface of  $\beta$ -Ga<sub>2</sub>O<sub>3</sub> single crystal by nitridation with NH<sub>3</sub>, Thin Solid Films 496 (1) (2006) 53–57. doi:10.1016/j.tsf.2005.08.230. URL <http://dx.doi.org/10.1016/j.tsf.2005.08.230>
- [13] Y. Tomm, P. Reiche, D. Klimm, T. Fukuda, Czochralski grown Ga<sub>2</sub>O<sub>3</sub> crystals, Journal of Crystal Growth 220 (4) (2000) 510–514. doi:10.1016/S0022-0248(00)00851-4. URL [http://dx.doi.org/10.1016/S0022-0248\(00\)00851-4](http://dx.doi.org/10.1016/S0022-0248(00)00851-4)

- [14] Z. Galazka, R. Uecker, D. Klimm, K. Irmscher, M. Naumann, M. Pietsch, A. Kwasniewski, R. Bertram, S. Ganschow, M. Bickermann, Scaling-Up of Bulk  $\beta$ -Ga<sub>2</sub>O<sub>3</sub> Single Crystals by the Czochralski Method, ECS Journal of Solid State Science and Technology 6 (2) (2017) Q3007–Q3011. doi:10.1149/2.0021702jss.  
URL <http://dx.doi.org/10.1149/2.0021702jss>
- [15] K. Hoshikawa, E. Ohba, T. Kobayashi, J. Yanagisawa, C. Miyagawa, Y. Nakamura, Growth of  $\beta$ -Ga<sub>2</sub>O<sub>3</sub> single crystals using vertical Bridgman method in ambient air, Journal of Crystal Growth 447 (2016) 36–41. doi:10.1016/j.jcrysgro.2016.04.022.  
URL <http://dx.doi.org/10.1016/j.jcrysgro.2016.04.022>
- [16] E. Ohba, T. Kobayashi, M. Kado, K. Hoshikawa, Defect characterization of  $\beta$ -Ga<sub>2</sub>O<sub>3</sub> single crystals grown by vertical Bridgman method, Japanese Journal of Applied Physics 55 (12) (2016) 1202BF. doi:10.7567/JJAP.55.1202BF.  
URL <http://dx.doi.org/10.7567/JJAP.55.1202BF>
- [17] H. Aida, K. Nishiguchi, H. Takeda, N. Aota, K. Sunakawa, Y. Yaguchi, Growth of  $\beta$ -Ga<sub>2</sub>O<sub>3</sub> Single Crystals by the Edge-Defined, Film Fed Growth Method, Japanese Journal of Applied Physics 47 (11) (2008) 8506–8509. doi:10.1143/JJAP.47.8506.  
URL <http://dx.doi.org/10.1143/JJAP.47.8506>
- [18] A. Kuramata, K. Koshi, S. Watanabe, Y. Yamaoka, T. Masui, S. Yamakoshi, High-quality  $\beta$ -Ga<sub>2</sub>O<sub>3</sub> single crystals grown by edge-defined film-fed growth, Japanese Journal of Applied Physics 55 (12) (2016) 1202A2. doi:10.7567/JJAP.55.1202A2.  
URL <http://dx.doi.org/10.7567/JJAP.55.1202A2>
- [19] M. Higashiwaki, K. Sasaki, A. Kuramata, T. Masui, S. Yamakoshi,

- Gallium oxide ( $\text{Ga}_2\text{O}_3$ ) metal-semiconductor field-effect transistors on single-crystal  $\beta$ - $\text{Ga}_2\text{O}_3$  (010)  
 Applied Physics Letters 100 (1) (2012) 013504. doi:10.1063/1.3674287.  
 URL <http://dx.doi.org/10.1063/1.3674287>
- [20] M. Higashiwaki, K. Sasaki, T. Kamimura, M. Hoi Wong, D. Krishnamurthy, A. Kuramata, T. Masui, S. Yamakoshi, Depletion-mode  $\text{Ga}_2\text{O}_3$  metal-oxide-semiconductor field-effect transistors on  $\beta$ - $\text{Ga}_2\text{O}_3$  (010) substrate  
 Applied Physics Letters 103 (12) (2013) 123511. doi:10.1063/1.4821858.  
 URL <http://dx.doi.org/10.1063/1.4821858>
- [21] K. D. Chabak, N. Moser, A. J. Green, D. E. Walker, S. E. Tetlak, E. Heller, A. Crespo, R. Fitch, J. P. McCandless, K. Leedy, M. Baldini, G. Wagner, Z. Galazka, X. Li, G. Jessen, Enhancement-mode  $\text{Ga}_2\text{O}_3$  wrap-gate fin field-effect transistors on native (100)  $\beta$ - $\text{Ga}_2\text{O}_3$  substrate  
 Applied Physics Letters 109 (21) (2016) 213501. doi:10.1063/1.4967931.  
 URL <http://dx.doi.org/10.1063/1.4967931>
- [22] A. J. Green, K. D. Chabak, E. R. Heller, R. C. Fitch, M. Baldini, A. Fiedler, K. Irmscher, G. Wagner, Z. Galazka, S. E. Tetlak, A. Crespo, K. Leedy, G. H. Jessen, 3.8-MV/cm Breakdown Strength of MOVPE-Grown Sn-Doped  $\beta$ - $\text{Ga}_2\text{O}_3$  MOSFETs,  
 IEEE Electron Device Letters 37 (7) (2016) 902–905.  
 doi:10.1109/LED.2016.2568139.  
 URL <http://dx.doi.org/10.1109/LED.2016.2568139>
- [23] M. H. Wong, K. Sasaki, A. Kuramata, S. Yamakoshi, M. Higashiwaki, Field-Plated  $\text{Ga}_2\text{O}_3$  MOSFETs With a Breakdown Voltage of Over 750 V,  
 IEEE Electron Device Letters 37 (2) (2016) 212–215.  
 doi:10.1109/LED.2015.2512279.  
 URL <http://dx.doi.org/10.1109/LED.2015.2512279>
- [24] N. A. Moser, J. P. McCandless, A. Crespo, K. D. Leedy, A. J. Green, E. R. Heller, K. D. Chabak, N. Peixoto, G. H. Jessen, High pulsed current density  $\beta$ - $\text{Ga}_2\text{O}_3$  MOSFETs verified by an analytical model corrected for interfac

- Applied Physics Letters 110 (14) (2017) 143505. doi:10.1063/1.4979789.  
URL <http://dx.doi.org/10.1063/1.4979789>
- [25] H. Zhou, K. Maize, G. Qiu, A. Shakouri, P. D. Ye,  
 $\beta$ -Ga<sub>2</sub>O<sub>3</sub> on insulator field-effect transistors with drain currents exceeding 1.5 A/mm and their self-heating,  
Applied Physics Letters 111 (9) (2017) 092102. doi:10.1063/1.5000735.  
URL <http://dx.doi.org/10.1063/1.5000735>
- [26] J. Noh, P. D. Ye, S. Alajlouni, M. J. Tadjer, J. C. Culbertson, H. Bae, M. Si, H. Zhou, P. A. Bermel, A. Shakouri,  
High Performance  $\beta$ -Ga<sub>2</sub>O<sub>3</sub> Nano-Membrane Field Effect Transistors on a High Thermal Conductivity Substrate,  
IEEE Journal of the Electron Devices Society 7 (June) (2019) 914–918.  
doi:10.1109/JEDS.2019.2933369.  
URL <http://dx.doi.org/10.1109/JEDS.2019.2933369>
- [27] H. Kim, S. Tarelkin, A. Polyakov, S. Troschiev, S. Nosukhin, M. Kuznetsov, J. Kim,  
Ultrawide-Bandgap p-n Heterojunction of Diamond/ $\beta$ -Ga<sub>2</sub>O<sub>3</sub> for a Solar-Blind Photodiode,  
ECS Journal of Solid State Science and Technology 9 (4) (2020) 045004.  
doi:10.1149/2162-8777/ab89b8.  
URL <http://dx.doi.org/10.1149/2162-8777/ab89b8>
- [28] Z. Guo, A. Verma, X. Wu, F. Sun, A. Hickman, T. Matsui, A. Kuramata, M. Higashiwaki, D. Jena, T. Luo,  
Anisotropic thermal conductivity in single crystal  $\beta$ -gallium oxide, Applied Physics Letters 106 (11) (2015) 1–6. doi:10.1063/1.4916078.  
URL <http://dx.doi.org/10.1063/1.4916078>
- [29] Sangmin Lee, R. Vetry, J. D. Brown, S. R. Gibb, W. Z. Cai, Jinming Sun, D. S. Green, J. Shealy,  
Reliability Assessment of AlGaIn/GaN HEMT Technology on SiC for 48V Applications,  
in: 2008 IEEE International Reliability Physics Symposium, IEEE, 2008,  
pp. 446–449. doi:10.1109/RELPHY.2008.4558926.  
URL <http://dx.doi.org/10.1109/RELPHY.2008.4558926>

- [30] J. W. Pomeroy, M. J. Uren, B. Lambert, M. Kuball,  
Operating Channel Temperature in GaN HEMTs: DC versus RF Accelerated Life Testing,  
Microelectronics Reliability 55 (12) (2015) 2505–2510.  
doi:10.1016/j.microrel.2015.09.025.  
URL <http://dx.doi.org/10.1016/j.microrel.2015.09.025>
- [31] Z. Cheng, L. Yates, J. Shi, M. J. Tadjer, K. D. Hobart, S. Graham,  
Thermal conductance across  $\beta$ -Ga<sub>2</sub>O<sub>3</sub>-diamond van der Waals heterogeneous interfaces,  
APL Materials 7 (3) (2019) 031118. doi:10.1063/1.5089559.  
URL <http://dx.doi.org/10.1063/1.5089559>
- [32] Z. Cheng, V. D. Wheeler, T. Bai, J. Shi, M. J. Tadjer,  
T. Feygelson, K. D. Hobart, M. S. Goorsky, S. Graham,  
Integration of polycrystalline Ga<sub>2</sub>O<sub>3</sub> on diamond for thermal management,  
Applied Physics Letters 116 (6) (2020) 062105. doi:10.1063/1.5125637.  
URL <http://dx.doi.org/10.1063/1.5125637>
- [33] T. Matsumae, Y. Kurashima, H. Umezawa,  
K. Tanaka, T. Ito, H. Watanabe, H. Takagi,  
Low-temperature direct bonding of  $\beta$ -Ga<sub>2</sub>O<sub>3</sub> and diamond substrates under atmospheric conditions,  
Applied Physics Letters 116 (14) (2020) 141602. doi:10.1063/5.0002068.  
URL <http://dx.doi.org/10.1063/5.0002068>
- [34] M. Schreck, S. Gsell, R. Brescia, M. Fischer,  
Ion bombardment induced buried lateral growth: the key mechanism for the synthesis of single crystal diamond,  
Scientific Reports 7 (1) (2017) 44462. doi:10.1038/srep44462.  
URL <http://dx.doi.org/10.1038/srep44462>
- [35] E. L. Thomas, G. W. Nelson, S. Mandal, J. S. Foord, O. a. Williams,  
Chemical mechanical polishing of thin film diamond, Carbon 68 (2014)  
473–479. doi:10.1016/j.carbon.2013.11.023.  
URL <http://dx.doi.org/10.1016/j.carbon.2013.11.023>
- [36] J. M. Werrell, S. Mandal, E. L. H. Thomas, E. B.  
Brousseau, R. Lewis, P. Borri, P. R. Davies, O. A. Williams,

- Effect of slurry composition on the chemical mechanical polishing of thin diamond films, *Science and Technology of Advanced Materials* 18 (1) (2017) 654–663.  
doi:10.1080/14686996.2017.1366815.  
URL <http://dx.doi.org/10.1080/14686996.2017.1366815>
- [37] S. Mandal, E. L. Thomas, L. Gines, D. Morgan, J. Green, E. B. Brousseau, O. A. Williams, Redox agent enhanced chemical mechanical polishing of thin film diamond, *Carbon* 130 (2018) 25–30. doi:10.1016/j.carbon.2017.12.077.  
URL <http://dx.doi.org/10.1016/j.carbon.2017.12.077>
- [38] S. Mandal, C. Yuan, F. Massabuau, J. W. Pomeroy, J. Cuenca, H. Bland, E. Thomas, D. Wallis, T. Batten, D. Morgan, R. Oliver, M. Kuball, O. A. Williams, Thick, Adherent Diamond Films on AlN with Low Thermal Barrier Resistance, *ACS Applied Materials & Interfaces* 11 (43) (2019) 40826–40834.  
doi:10.1021/acsami.9b13869.  
URL <http://dx.doi.org/10.1021/acsami.9b13869>
- [39] W. D. Harkins, Energy Relations of the Surface of Solids I. Surface Energy of the Diamond, *The Journal of Chemical Physics* 10 (5) (1942) 268–272.  
doi:10.1063/1.1723719.  
URL <http://dx.doi.org/10.1063/1.1723719>
- [40] R. J. Jaccodine, Surface Energy of Germanium and Silicon, *Journal of The Electrochemical Society* 110 (6) (1963) 524. doi:10.1149/1.2425806.  
URL <http://dx.doi.org/10.1149/1.2425806>
- [41] O. Williams, Nanocrystalline diamond, *Diamond and Related Materials* 20 (5-6) (2011) 621–640. doi:10.1016/j.diamond.2011.02.015.  
URL <http://dx.doi.org/10.1016/j.diamond.2011.02.015>
- [42] S. Mandal, Nucleation of diamond films on heterogeneous substrates: a review, *RSC Advances* 11 (2021) 10159–10182. doi:10.1039/D1RA00397F.  
URL <https://doi.org/10.1039/D1RA00397F>

- [43] V. Bermudez, The structure of low-index surfaces of  $\beta$ -Ga<sub>2</sub>O<sub>3</sub>, Chemical Physics 323 (2-3) (2006) 193–203. doi:10.1016/j.chemphys.2005.08.051. URL <http://dx.doi.org/10.1016/j.chemphys.2005.08.051>
- [44] A. Y. Polyakov, I.-H. Lee, N. B. Smirnov, E. B. Yakimov, I. V. Shchemerov, A. V. Chernykh, A. I. Kochkova, A. A. Vasilev, F. Ren, P. H. Carey, S. J. Pearton, Hydrogen plasma treatment of  $\beta$ -Ga<sub>2</sub>O<sub>3</sub>: Changes in electrical properties and deep trap spectra, Applied Physics Letters 115 (3) (2019) 032101. doi:10.1063/1.5108790. URL <http://aip.scitation.org/doi/10.1063/1.5108790>
- [45] R. Van Wagenen, J. Andrade, Flat plate streaming potential investigations: Hydrodynamics and electrokinetics, Journal of Colloid and Interface Science 76 (2) (1980) 305–314. doi:10.1016/0021-9797(80)90374-4. URL [https://doi.org/10.1016/0021-9797\(80\)90374-4](https://doi.org/10.1016/0021-9797(80)90374-4)
- [46] A. Voigt, H. Wolf, S. Lauekner, G. Neumann, R. Becker, L. Richter, Electrokinetic properties of polymer and glass surfaces in aqueous solutions: Experimental evidence for surface charges, Biomaterials 4 (4) (1983) 299–304. doi:10.1016/0142-9612(83)90032-7. URL <http://linkinghub.elsevier.com/retrieve/pii/0142961283900327>
- [47] W. Norde, E. Rouwendal, Streaming potential measurements as a tool to study protein adsorption kinetics, Journal of Colloid and Interface Science 139 (1) (1990) 169–176. doi:10.1016/0021-9797(90)90454-V. URL <http://linkinghub.elsevier.com/retrieve/pii/002197979090454V>
- [48] P. J. Scales, F. Grieser, T. W. Healy, Electrokinetics of the muscovite mica-aqueous solution interface, Langmuir 6 (3) (1990) 582–589. doi:10.1021/la00093a012. URL <http://pubs.acs.org/doi/abs/10.1021/la00093a012>
- [49] S. Mandal, E. L. H. Thomas, C. Middleton, L. Gines, J. T. Griffiths, M. J. Kappers, R. A. Oliver, D. J. Wallis, L. E. Goff, S. A. Lynch, M. Kuball, O. A. Williams,



Surface Zeta Potential and Diamond Seeding on Gallium Nitride Films,  
 ACS Omega 2 (10) (2017) 7275–7280. arXiv:1707.05410,  
 doi:10.1021/acsomega.7b01069.

URL <http://pubs.acs.org/doi/10.1021/acsomega.7b01069>

- [50] H. A. Bland, E. L. H. Thomas, G. M. Klemencic, S. Mandal,  
 D. J. Morgan, A. Papageorgiou, T. G. Jones, O. A. Williams,  
 Superconducting Diamond on Silicon Nitride for Device Applications, Sci-  
 entific Reports 9 (1) (2019) 2911. doi:10.1038/s41598-019-39707-z.  
 URL <http://dx.doi.org/10.1038/s41598-019-39707-z>

- [51] S. Mandal, H. A. Bland, J. A. Cuenca, M. Snowball, O. Williams,  
 Superconducting boron doped nanocrystalline diamond on boron nitride ceramics,  
 Nanoscale 11 (2019) 10266. doi:10.1039/C9NR02729G.  
 URL <http://dx.doi.org/10.1039/C9NR02729G>

- [52] H. A. Bland, I. A. Centeleghe, S. Mandal,  
 E. L. H. Thomas, J.-y. Maillard, O. A. Williams,  
 Electropositive Nanodiamond-Coated Quartz Microfiber Membranes for Virus and Dye Filtration,  
 ACS Applied Nano Materials 4 (3) (2021) 3252–3261.  
 doi:10.1021/acsanm.1c00439.  
 URL <https://pubs.acs.org/doi/10.1021/acsanm.1c00439>

- [53] C. Werner, H. Körber, R. Zimmermann, S. Dukhin, H.-J. Ja-  
 cobasch, Extended Electrokinetic Characterization of Flat Solid Surfaces,  
 Journal of Colloid and Interface Science 208 (1) (1998) 329–346.  
 doi:10.1006/jcis.1998.5787.  
 URL <http://linkinghub.elsevier.com/retrieve/pii/S0021979798957873>

- [54] S. B. S. Heil, J. L. van Hemmen, C. J. Hodson, N. Singh, J. H.  
 Klootwijk, F. Roozeboom, M. C. M. van de Sanden, W. M. M. Kessels,  
 Deposition of TiN and HfO<sub>2</sub> in a commercial 200 mm remote plasma atomic layer deposition reactor,  
 Journal of Vacuum Science & Technology A: Vacuum, Surfaces, and Films

25 (5) (2007) 1357. doi:10.1116/1.2753846.

URL <http://scitation.aip.org/content/avs/journal/jvsta/25/5/10.1116/1.2753846>

- [55] E. Langereis, S. B. S. Heil, H. C. M. Knoops, W. Keuning, M. C. M. van de Sanden, W. M. M. Kessels, In situ spectroscopic ellipsometry as a versatile tool for studying atomic layer deposition, *Journal of Physics D: Applied Physics* 42 (7) (2009) 073001. doi:10.1088/0022-3727/42/7/073001. URL <https://iopscience.iop.org/article/10.1088/0022-3727/42/7/073001>

- [56] J. Hees, A. Kriele, O. A. Williams, Electrostatic self-assembly of diamond nanoparticles, *Chemical Physics Letters* 509 (1-3) (2011) 12–15. doi:10.1016/j.cplett.2011.04.083. URL <https://doi.org/10.1016/j.cplett.2011.04.083>

- [57] M. Kosmulski, Pristine Points of Zero Charge of Gallium and Indium Oxides, *Journal of Colloid and Interface Science* 238 (1) (2001) 225–227. doi:10.1006/jcis.2001.7484. URL <https://linkinghub.elsevier.com/retrieve/pii/S0021979701974843>

- [58] G. Chen, Z. Ni, Y. Bai, Q. Li, Y. Zhao, The role of interactions between abrasive particles and the substrate surface in chemical-mechanical planarization, *RSC Advances* 7 (28) (2017) 16938–16952. doi:10.1039/C6RA27508G. URL <https://doi.org/10.1039/C6RA27508G>

- [59] J. L. Reyes Bahena, A. Robledo Cabrera, A. López Valdivieso, R. Herrera Urbina, Fluoride adsorption onto  $\alpha$ -Al<sub>2</sub>O<sub>3</sub> and its effect on the zeta potential at the alumina–aqueous electrolyte interface, *Separation Science and Technology* 37 (8) (2002) 1973–1987. doi:10.1081/SS-120003055. URL <https://doi.org/10.1081/SS-120003055>

- [60] J. W. Lee, B. Pathangey, M. R. Davidson, P. H. Holloway, E. S. Lambers, B. Davydov, T. J. Anderson, S. J. Pearton,

- Comparison of plasma chemistries for dry etching thin film electroluminescent display materials, *Journal of Vacuum Science & Technology A: Vacuum, Surfaces, and Films* 16 (4) (1998) 2177–2186. doi:10.1116/1.581326.  
URL <http://avs.scitation.org/doi/10.1116/1.581326>
- [61] B. Lee, T. R. Hayes, P. M. Thomas, R. Pawelek, P. F. Sciortino, SiO<sub>2</sub> mask erosion and sidewall composition during CH<sub>4</sub>/H<sub>2</sub> reactive ion etching of InGaAsP/InP, *Applied Physics Letters* 63 (23) (1993) 3170–3172.  
doi:10.1063/1.110213.  
URL <http://aip.scitation.org/doi/10.1063/1.110213>
- [62] D. Dohy, G. Lucazeau, A. Revcolevschi, Raman spectra and valence force field of single-crystalline  $\beta$  Ga<sub>2</sub>O<sub>3</sub>, *Journal of Solid State Chemistry* 45 (2) (1982) 180–192.  
doi:10.1016/0022-4596(82)90274-2.  
URL [https://doi.org/10.1016/0022-4596\(82\)90274-2](https://doi.org/10.1016/0022-4596(82)90274-2)
- [63] C. Kranert, C. Sturm, R. Schmidt-Grund, M. Grundmann, Raman tensor elements of  $\beta$ -Ga<sub>2</sub>O<sub>3</sub>, *Scientific Reports* 6 (2016) 1–9.  
doi:10.1038/srep35964.  
URL <http://dx.doi.org/10.1038/srep35964>
- [64] J. Olivero, R. Longbothum, Empirical fits to the Voigt line width: A brief review, *Journal of Quantitative Spectroscopy and Radiative Transfer* 17 (2) (1977) 233–236. doi:10.1016/0022-4073(77)90161-3.  
URL [https://doi.org/10.1016/0022-4073\(77\)90161-3](https://doi.org/10.1016/0022-4073(77)90161-3)
- [65] P. M. Sherwood, Rapid evaluation of the Voigt function and its use for interpreting X-ray photoelectron spectra, *Surface and Interface Analysis* 51 (2) (2019) 254–274.  
doi:10.1002/sia.6577.  
URL <https://doi.org/10.1002/sia.6577>
- [66] A. Dychalska, K. Fabisiak, K. Paprocki, J. Makowiecki, A. Iskalyeva, M. Szybowicz,

- A Raman spectroscopy study of the effect of thermal treatment on structural and photoluminescence properties of diamond-like carbon films, *Materials & Design* 112 (2016) 320–327.  
doi:10.1016/j.matdes.2016.09.092.  
URL <https://doi.org/10.1016/j.matdes.2016.09.092>
- [67] P. W. May, J. A. Smith, K. N. Rosser, 785 nm Raman Spectroscopy of CVD Diamond Films, *MRS Online Proceedings Library* 1039 (1) (2007) 1502. doi:10.1557/PROC-1039-P15-02.  
URL <https://doi.org/10.1557/PROC-1039-P15-02>
- [68] A. C. Ferrari, J. Robertson, Resonant Raman spectroscopy of disordered, amorphous, and diamondlike carbon, *Physical Review B* 64 (7) (2001) 075414.  
doi:10.1103/PhysRevB.64.075414.  
URL <http://link.aps.org/doi/10.1103/PhysRevB.64.075414>
- [69] A. C. Ferrari, J. Robertson, Raman spectroscopy of amorphous, nanostructured, diamond-like carbon, and nanotubes, *Philosophical Transactions of the Royal Society of London. Series A: Mathematical, Physical and Engineering Sciences* 362 (1824) (2004) 2477–2512.  
doi:10.1098/rsta.2004.1452.  
URL <https://doi.org/10.1098/rsta.2004.1452>
- [70] S. Praver, R. J. Nemanich, Raman spectroscopy of diamond and doped diamond, *Philosophical Transactions of the Royal Society of London. Series A: Mathematical, Physical and Engineering Sciences* 362 (1824) (2004) 2537–2565.  
doi:10.1098/rsta.2004.1451.  
URL <https://doi.org/10.1098/rsta.2004.1451>
- [71] C. Ramaswamy, Raman Effect in Diamond, *Nature* 125 (1930) 704–704.  
doi:10.1038/125704b0.  
URL <https://doi.org/10.1038/125704b0>
- [72] S. Bhagavantam, Relation of Raman Effect to Crystal Structure, *Indian Journal of Physics* 5 (1930) 169.  
URL <http://hdl.handle.net/10821/555>

- [73] D. S. Knight, W. B. White, Characterization of diamond films by Raman spectroscopy, Journal of Materials Research 4 (2) (1989) 385–393.  
doi:10.1557/JMR.1989.0385.  
URL <http://link.springer.com/10.1557/JMR.1989.0385>
- [74] J. W. Ager, M. D. Drory, Quantitative measurement of residual biaxial stress by Raman spectroscopy in diamond, Physical Review B 48 (4) (1993) 2601–2607.  
doi:10.1103/PhysRevB.48.2601.  
URL <https://doi.org/10.1103/PhysRevB.48.2601>
- [75] H. Windischmann, K. Gray, Stress measurement of CVD diamond films, Diamond and Related Materials 4 (5-6) (1995) 837–842.  
doi:10.1016/0925-9635(94)05327-8.  
URL [https://doi.org/10.1016/0925-9635\(94\)05327-8](https://doi.org/10.1016/0925-9635(94)05327-8)
- [76] E. Anastassakis, Strain characterization of polycrystalline diamond and silicon systems, Journal of Applied Physics 86 (1) (1999) 249–258. doi:10.1063/1.370723.  
URL <https://doi.org/10.1063/1.370723>
- [77] A. Dychalska, K. Fabisiak, K. Paprocki, A. Dudkowiak, M. Szybowicz, Temperature dependence of stress in CVD diamond films studied by Raman spectroscopy, Materials Science- Poland 33 (3) (2015) 620–626.  
doi:10.1515/msp-2015-0064.  
URL <https://doi.org/10.1515/msp-2015-0064>
- [78] T. Gries, L. Vandenbulcke, P. Simon, A. Canizares, Stresses in textured and polycrystalline cubic films by Raman spectroscopy: Application to diamond, Journal of Applied Physics 102 (8) (2007). doi:10.1063/1.2798940.  
URL <https://doi.org/10.1063/1.2798940>
- [79] H. Boppart, J. van Straaten, I. F. Silvera, Raman spectra of diamond at high pressures, Physical Review B 32 (2) (1985) 1423–1425. doi:10.1103/PhysRevB.32.1423.  
URL <https://link.aps.org/doi/10.1103/PhysRevB.32.1423>

- [80] M. Yoshikawa, G. Katagiri, H. Ishida, A. Ishitani, M. Ono, K. Matsumura,  
Characterization of crystalline quality of diamond films by Raman spectroscopy,  
Applied Physics Letters 55 (25) (1989) 2608–2610.  
doi:10.1063/1.101951.  
URL <http://aip.scitation.org/doi/10.1063/1.101951>
- [81] M. Yoshikawa, H. Ishida, A. Ishitani, S. Koizumi, T. Inuzuka,  
Study of crystallographic orientations in the diamond film on the (100) surface of cubic boron nitride using  
Applied Physics Letters 58 (13) (1991) 1387–1388.  
doi:10.1063/1.104316.  
URL <https://doi.org/10.1063/1.104316>
- [82] J. A. Cuenca, M. D. Smith, D. E. Field, F. C-  
P. Massabuau, S. Mandal, J. Pomeroy, D. J. Wallis,  
R. A. Oliver, I. Thayne, M. Kuball, O. A. Williams,  
Thermal stress modelling of diamond on GaN/III-Nitride membranes,  
Carbon 174 (2021) 647–661. doi:10.1016/j.carbon.2020.11.067.  
URL <https://doi.org/10.1016/j.carbon.2020.11.067>
- [83] A. C. Ferrari, J. Robertson, Origin of the  $1150\text{ cm}^{-1}$  Raman mode in nanocrystalline diamond,  
Physical Review B 63 (12) (2001) 121405.  
doi:10.1103/PhysRevB.63.121405.  
URL <https://link.aps.org/doi/10.1103/PhysRevB.63.121405>
- [84] P. Pavone, K. Karch, O. Schütt, D. Strauch, W. Windl, P. Giannozzi,  
S. Baroni, Ab initio lattice dynamics of diamond, Physical Review B 48 (5)  
(1993) 3156–3163. doi:10.1103/PhysRevB.48.3156.  
URL <https://link.aps.org/doi/10.1103/PhysRevB.48.3156>

## Supporting Information: Surface zeta potential and diamond growth on gallium oxide single crystal

### S1. Raman Spectroscopy

Table S1 shows the peak position and FWHM of the Raman peaks as determined by Voigtian peak fitting. GLmix is defined as  $\frac{\text{FWHM}(\text{Lorentz})}{\text{FWHM}(\text{Lorentz}) + \text{FWHM}(\text{Gauss})}$ . This means that a pure Lorentzian profile will give a GLmix of 1 and a pure Gaussian will give the value of 0.

Figure S1 and S2 shows the Raman spectroscopy data taken with 473nm and 660nm excitation laser respectively. The data on bare  $\beta\text{-Ga}_2\text{O}_3$  is shown in black and the red curves are for data on  $\text{SiO}_2$  coated  $\beta\text{-Ga}_2\text{O}_3$ . The change in relative intensities of various peaks are clearly visible between bare substrate and  $\text{SiO}_2$  coated substrate.

Raman spectroscopy data comparing  $\beta\text{-Ga}_2\text{O}_3$ ,  $\text{SiO}_2$  coated  $\beta\text{-Ga}_2\text{O}_3$  and diamond grown on  $\text{SiO}_2$  coated  $\beta\text{-Ga}_2\text{O}_3$  are shown in figure S3. The  $\beta\text{-Ga}_2\text{O}_3$  peaks can be clearly seen all three spectra confirming the  $\beta\text{-Ga}_2\text{O}_3$  layer under the diamond. Figure S4 shows the Raman data of thin diamond film grown on  $\text{SiO}_2$  coated  $\beta\text{-Ga}_2\text{O}_3$ . A straight line background has been subtracted from the data taken with 473 and 532nm excitation laser. The data clearly shows the presence of the  $\beta\text{-Ga}_2\text{O}_3$  peaks in the low frequency regime.

Raman mode	$\beta$ -Ga <sub>2</sub> O <sub>3</sub>				SiO <sub>2</sub> on $\beta$ -Ga <sub>2</sub> O <sub>3</sub>			
	Peak Center	FWHM	GLmix	Rel. Int.	Peak Center	FWHM	GLmix	Rel. Int.
A1	110.29	1.69	0.56	5.23	110.86	2.21	0.35	6.36
B1	113.89	1.38	0.16	28.58	114.24	1.76	0.21	16.49
B2	144.54	3.22	0.73	161.81	144.92	3.51	0.65	80.70
A2	169.45	1.80	0.43	185.33	169.84	1.97	0.42	191.48
A3	199.99	1.85	0.45	1000	200.41	2.06	0.42	1000
A4	319.84	6.19	0.53	88.01	320.36	6.22	0.66	272.59
A5, B3	346.40	6.03	1.00	485.66	347.01	6.02	0.87	468.66
A6	416.28	3.36	0.71	422.81	416.75	3.50	0.68	792.22
A7, B4	475.03	9.76	0.92	296.33	475.15	10.25	0.75	69.62
A8	629.70	6.50	1.00	118.22	630.62	6.91	0.92	33.10
B5	651.88	3.46	1.00	139.91	652.32	3.54	0.78	64.48
A9	657.95	6.87	1.00	62.65	658.50	6.81	0.86	710.74
A10	766.20	8.43	1.00	15.90	766.53	9.78	0.80	343.70

Table S1: Position of various Raman modes in  $\beta$ -Ga<sub>2</sub>O<sub>3</sub> and SiO<sub>2</sub>covered  $\beta$ -Ga<sub>2</sub>O<sub>3</sub> along with their FWHM and relative intensities with respect to A3 mode. The peak positions and FWHM are in cm<sup>-1</sup>.



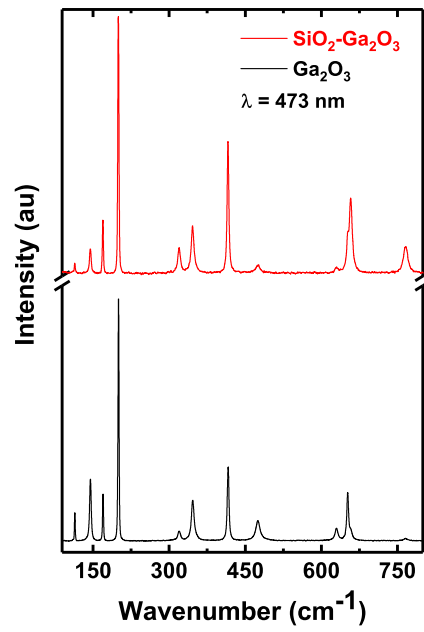


Figure S1: Raman spectroscopy data is shown for  $\beta\text{-Ga}_2\text{O}_3$  (black curve) and  $\text{SiO}_2$  covered  $\beta\text{-Ga}_2\text{O}_3$  (red curve) taken with 473 nm laser.

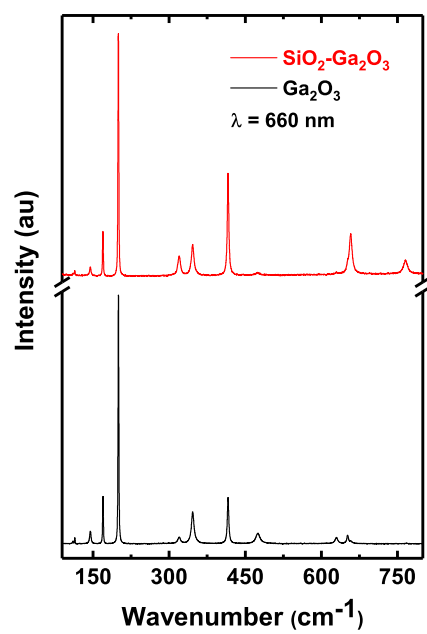


Figure S2: Raman spectroscopy data is shown for  $\beta\text{-Ga}_2\text{O}_3$  (black curve) and  $\text{SiO}_2$  covered  $\beta\text{-Ga}_2\text{O}_3$  (black curve) taken with 660 nm laser.

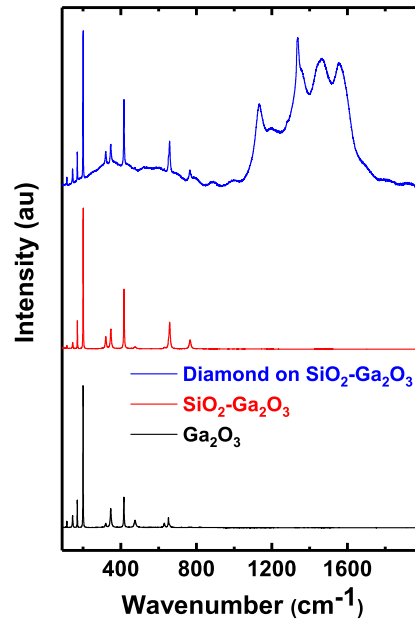


Figure S3: Raman spectroscopy data is shown for  $\beta$ -Ga<sub>2</sub>O<sub>3</sub>, SiO<sub>2</sub>covered  $\beta$ -Ga<sub>2</sub>O<sub>3</sub> and diamond grown on SiO<sub>2</sub>covered  $\beta$ -Ga<sub>2</sub>O<sub>3</sub> taken using 532 nm laser. The peaks for  $\beta$ -Ga<sub>2</sub>O<sub>3</sub> are clearly seen along with diamond peaks in the data.

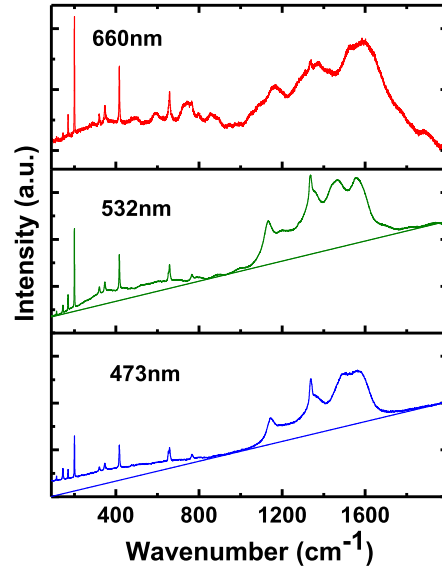


Figure S4: Raman spectroscopy data is shown for diamond grown on SiO<sub>2</sub>covered  $\beta$ -Ga<sub>2</sub>O<sub>3</sub> taken using 473, 532 and 660 nm laser. The peaks for  $\beta$ -Ga<sub>2</sub>O<sub>3</sub> are clearly seen along with diamond peaks in the data. A straight line background has been subtracted from the data taken by 473 and 532 nm excitation laser as indicated in the figure.